

Direct Synthesis of Ammonia from Nitrate on Amorphous Graphene with Near 100% Efficiency

Libei Huang, Le Cheng, Tinghao Ma, Jun-Jie Zhang,* Haikun Wu, Jianjun Su, Yun Song, He Zhu, Qi Liu, Minghui Zhu, Zhiyuan Zeng, Qiyuan He, Man-Kit Tse, Deng-tao Yang, Boris I. Yakobson,* Ben Zhong Tang, Yang Ren, and Ruquan Ye*

Ammonia is an indispensable commodity in the agricultural and pharmaceutical industries. Direct nitrate-to-ammonia electroreduction is a decentralized route yet challenged by competing side reactions. Most catalysts are metal-based, and metal-free catalysts with high nitrate-to-ammonia conversion activity are rarely reported. Herein, it is shown that amorphous graphene synthesized by laser induction and comprising strained and disordered pentagons, hexagons, and heptagons can electrocatalyze the eight-electron reduction of NO_3^- to NH_3 with a Faradaic efficiency of $\approx 100\%$ and an ammonia production rate of $2859 \mu\text{g cm}^{-2} \text{h}^{-1}$ at -0.93 V versus reversible hydrogen electrode. X-ray pair-distribution function analysis and electron microscopy reveal the unique molecular features of amorphous graphene that facilitate NO_3^- reduction. In situ Fourier transform infrared spectroscopy and theoretical calculations establish the critical role of these features in stabilizing the reaction intermediates via structural relaxation. The enhanced catalytic activity enables the implementation of flow electrolysis for the on-demand synthesis and release of ammonia with $>70\%$ selectivity, resulting in significantly increased yields and survival rates when applied to plant cultivation. The results of this study show significant promise for remediating nitrate-polluted water and completing the NO_x cycle.

1. Introduction

Ammonia is an important chemical widely used as a fertilizer and in the manufacture of many nitrogen-containing compounds.^[1] Because of its greater energy density and lower transportation cost than hydrogen,^[2] ammonia is also regarded as a promising next-generation energy carrier.^[3] The Haber–Bosch process, which catalyzes the reaction of nitrogen with hydrogen at temperatures of $400\text{--}600 \text{ }^\circ\text{C}$ and pressures above 100 bar ,^[4,5] has been the main industrial process for ammonia production for more than a century. Because of the energy- and resource-intensive character of the Haber–Bosch method, electrochemical synthesis of ammonia via the nitrogen reduction reaction and plasmon-enabled nitrogen activation using renewable electricity are regarded as promising approaches to decarbonize the NH_3 market.^[6] However, the high dissociation energy of the $\text{N}\equiv\text{N}$ bond (941 kJ mol^{-1})

L. Huang, L. Cheng, H. Wu, J. Su, Y. Song, M.-K. Tse, R. Ye
Department of Chemistry
State Key Laboratory of Marine Pollution
City University of Hong Kong
Hong Kong 999077, P. R. China
E-mail: ruquanye@cityu.edu.hk

L. Huang
Division of Science
Engineering and Health Study
School of Professional Education and Executive Development
(PolyU SPEED)
The Hong Kong Polytechnic University
Hong Kong 999077, P. R. China


T. Ma, D.-t. Yang
School of Chemistry and Chemical Engineering
Northwestern Polytechnical University
Xi'an 710072, P. R. China

J.-J. Zhang, B. I. Yakobson
Department of Materials Science and Nano Engineering and Department
of Chemistry
Rice University
6100 Main Street, Houston, TX 77005, USA
E-mail: jz73@rice.edu; biy@rice.edu

H. Zhu, Q. Liu, Y. Ren
Department of Physics
City University of Hong Kong
Hong Kong 999077, P. R. China

M. Zhu
State Key Laboratory of Chemical Engineering
East China University of Science and Technology
Shanghai 200237, P. R. China

Z. Zeng, Q. He
Department of Materials Science and Engineering
City University of Hong Kong
Hong Kong 999077, P. R. China

 The ORCID identification number(s) for the author(s) of this article can be found under <https://doi.org/10.1002/adma.202211856>

© 2023 The Authors. Advanced Materials published by Wiley-VCH GmbH. This is an open access article under the terms of the Creative Commons Attribution License, which permits use, distribution and reproduction in any medium, provided the original work is properly cited.

DOI: 10.1002/adma.202211856

and the low solubility of nitrogen impede the efficient production of ammonia.^[7]

Nitrate electroreduction has recently received attention as a decentralized means of ammonia synthesis.^[8] Although this method cannot compete with the centralized Haber–Bosch method, it provides a decentralized route to remediate nitrate waste. Nitrate reduction has advantages over N₂ reduction due to the relatively low dissociation energy of the N=O bond (204 kJ mol⁻¹) and the greater solubility of NO₃⁻.^[1,4] Plasma chemistry converting N₂ to nitrous species can also provide readily available sources of nitrate.^[9–11] Moreover, abundant nitrate is available in discharged wastewater and polluted groundwaters, where the NO₃⁻ concentration can be as high as 41.6 mM in industrial wastewater and 1.95 M in low-level nuclear wastewater.^[8] The nitrate in eutrophicated and contaminated water sources poses health risks to humans and wildlife.^[12] Early studies primarily used denitrification to reduce NO₃⁻ to N₂.^[13–16] However, the direct electrochemical reduction of nitrate waste to value-added products has greater practical significance in terms of the environment and economy. Current nitrate reduction catalysts are primarily metals, alloys, or metal oxides, such as Ti,^[12] TiO₂,^[17] Ru,^[4] Fe,^[7] Cu–Ni alloy,^[18] CuO,^[3,6] and a Cu–molecular composite.^[1] Although nonmetallic materials such as graphite felt,^[19] carbon paper,^[20,21] and boron-doped diamond^[22,23] have been examined in this regard, the presence of competing nitrate reduction pathways and the hydrogen evolution side reaction limit their use in the direct reduction of nitrate to ammonia. Thus, highly efficient nitrate-to-ammonia conversion remains an enduring challenge for nonmetal catalysts.

Herein, we report that amorphous graphene comprising disordered four-, five-, six-, seven-, and eight-membered ring structures can electrocatalyze the conversion of nitrate to ammonia with 94.3% Faradaic efficiency (FE). This result is the first reported example of a metal-free material with comparable or superior nitrate-to-NH₃ selectivity relative to metal-based catalysts. Our amorphous graphene is synthesized by laser irradiation of a polyimide polymer in air or under an inert atmosphere, which favors the formation of polygonal structures due to kinetic effects. The amorphous graphenes obtained by laser induction in air and under an inert atmosphere are denoted as ox-LIG and LIG, respectively. Reduced graphene oxide (rGO), which has a similar morphology but higher crystallinity, is synthesized by a modified Hummers' method for comparison. Atomic pair distribution function (PDF) analysis, electron paramagnetic resonance (EPR) spectroscopy, and high-resolution transmission electron microscopy (HRTEM) establish distinct structural characteristics

of ox-LIG and LIG relative to those of rGO. LIG and ox-LIG exhibit an enhanced FE of nitrate-to-NH₃ conversion relative to rGO. The amorphous graphene FE exceeds 80% over a wide potential range and reaches a maximum value of nearly 100% at -0.93 V versus reversible hydrogen electrode (RHE) with an ammonia production rate of ≈3000 μg cm⁻² h⁻¹. In situ Fourier-transform infrared (FTIR) spectroscopy and density functional theory (DFT) calculations reveal the essential role of amorphous carbon in directing the catalytic selectivity. The degree of oxidation of amorphous graphene also affects selectivity. LIG, which has an amorphous structure with lower oxygen content, shows poorer activity than ox-LIG. Our work describes the uncommonly high nitrate reduction activity of amorphous graphene and its potential for application in wastewater remediation and the agricultural industry. We also show that electroreduced nitrate electrolyte can be used to cultivate vegetables and significantly increase crop yields.

2. Results and Discussion

2.1. Preparation and Characterization of Graphene Materials

Amorphous graphene and conventional rGO were synthesized as shown in Figure 1a. ox-LIG and LIG were formed directly from polyimide by CO₂-laser irradiation in ambient air and under a nitrogen atmosphere, respectively. The local temperature due to the photothermal effect during laser irradiation can be as high as 2500 °C.^[24] The scanning electron microscopy (SEM) images in Figure S1 (Supporting Information) reveal the extensive porosity of ox-LIG and LIG, which is caused by the rapid release of gaseous products.^[25] The porous structure exhibits a large specific surface area,^[24] which is crucial for catalytic applications. The transmission electron microscopy (TEM) images in Figure S2 (Supporting Information) show that the ox-LIG and LIG structures comprise only a few layers. Graphene oxide (GO) was prepared by a modified Hummers' method.^[26–28] rGO was prepared by thermal reduction of GO. The TEM images of rGO in Figure S2 (Supporting Information) show single-layered and wrinkled structures. X-ray photoelectron spectroscopy (XPS, Figure S3a, Supporting Information) shows that the oxygen content of ox-LIG is greater than that of LIG and rGO with more C–O and O–C=O bonds in ox-LIG revealed by deconvolution analysis. The 291.02 eV binding energy peak in LIG is assigned to π–π* shakeup of the aromatic sp² carbons.^[29] Figure S3b (Supporting Information) shows ≈148° and ≈20° contact angles for hydrophobic LIG and hydrophilic ox-LIG, respectively, which correlates with their surface properties. Raman spectra of ox-LIG, LIG, and rGO are depicted in Figure S4 (Supporting Information). Three characteristic signals at ≈1352 (D peak), ≈1589 (G peak), and ≈2700 cm⁻¹ (2D peak) are observed.^[30,31] The G-peak to 2D-peak intensity ratios (*I_G/I_{2D}*) of ox-LIG and LIG are 2.7 and 2.03, respectively, which indicates that the materials comprise but a few layers^[32] in accord with the TEM images in Figure S2 (Supporting Information). The intensity of the 2D peak of rGO is relatively low, which may result from wrinkles and layer lamination in the very thin material (Figure S2, Supporting Information).^[33–36] A larger D-peak to G-peak intensity ratio (*I_D/I_G*) usually signifies a greater degree of disorder in carbon materials.^[33,37] The larger *I_D/I_G* of ox-LIG relative to LIG may arise from its greater degree of oxidation.

B. Z. Tang
School of Science and Engineering
Shenzhen Institute of Aggregate Science and Technology
The Chinese University of Hong Kong
Shenzhen, Guangdong 518172, P. R. China
Y. Ren
X-Ray Science Division
Argonne National Laboratory
9700 S. Cass Ave., Argonne, IL 60439, USA
R. Ye
City University of Hong Kong Shenzhen Research Institute
Shenzhen, Guangdong 518057, China

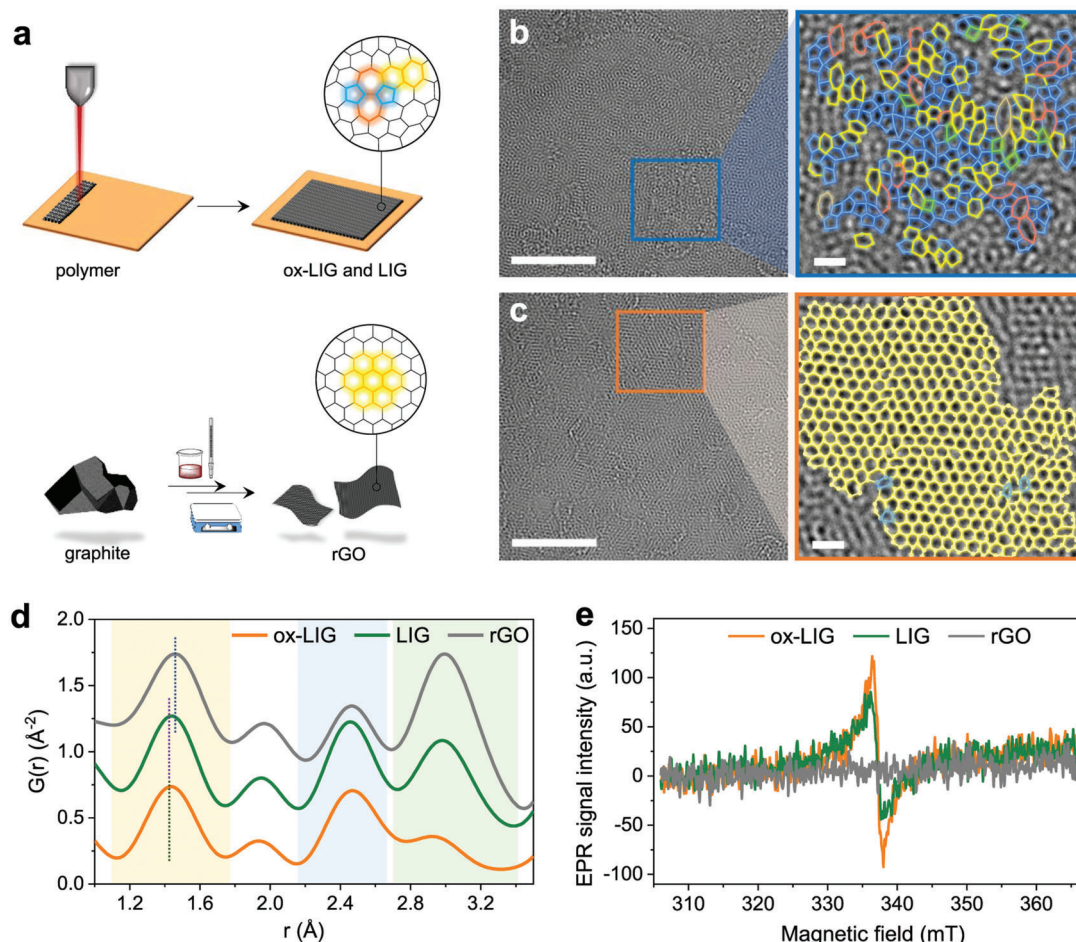


Figure 1. Preparation and characterization of ox-LIG, LIG, and rGO. a) Schematic of the preparation of ox-LIG, LIG, and rGO. b,c) HRTEM images of ox-LIG (b) and rGO (c). Scale bars equal 5 and 0.5 nm in the normal and enlarged areas, respectively. Four-, five-, six-, seven-, and eight-membered rings are highlighted in green, blue, yellow, red, and light brown, respectively. d) PDF analyses and e) EPR signals of ox-LIG, LIG, and rGO.

The X-ray diffraction (XRD) pattern in Figure S5 (Supporting Information) contains peaks corresponding to the (002) and (100) facets. The (002) peaks of ox-LIG and LIG are located at $2\theta = 26^\circ$, whereas $2\theta = 23^\circ$ for rGO. This difference suggests a larger d -spacing in rGO than in ox-LIG and LIG.^[38] The FTIR spectra in Figure S6 (Supporting Information) show the presence of C–O ($1024\text{--}1043\text{ cm}^{-1}$), C–OH ($1144\text{--}1163\text{ cm}^{-1}$), and C=C ($\approx 1640\text{ cm}^{-1}$) bonds in all samples. The vibrational mode at $\approx 3438\text{ cm}^{-1}$ is from the O–H bond of water.^[39]

The HRTEM images in Figure 1b,c reveal distinctly different carbon lattices in ox-LIG and rGO. Figure 1b shows that the rGO structure comprises predominantly strained hexagons with sporadic pentagons, whereas significantly different lattices are observed in ox-LIG and LIG. The ox-LIG (Figure 1c) and LIG (Figure S7, Supporting Information) structures contain primarily five-, six-, and seven-membered rings embedded with a few four- and eight-membered rings. The hexagons in ox-LIG and LIG are severely distorted. The irregular atomic structure with abundant disorders and grain boundaries establishes the amorphous nature of ox-LIG and LIG. PDF analysis provides statistical insight into the interatomic distances in rGO, ox-LIG, and LIG. All samples show three characteristic graphene bands with the nearest

planar pair distances (r) of ≈ 1.42 , 2.46 , and 2.84 \AA (Figure 1d) and a minor peak at $r = 1.97\text{ \AA}$ from the interlayer sp^3 bonds.^[40–42] The nearest-neighbor bond distance in rGO is 1.46 \AA , whereas it is 1.44 \AA in both ox-LIG and LIG, which reflects the different degrees of strain in the three materials. The shorter carbon–carbon distance in ox-LIG and LIG may arise from the formation of multiple Stone–Wales defects due to rapid heating and cooling during laser irradiation.^[42] The room-temperature EPR signal (Figure 1e) demonstrates the presence of a small population of unpaired electrons in the rGO structure, in accordance with recent literature.^[42] However, a distinct EPR signal is observed in ox-LIG and LIG, which indicates the existence of abundant radicals.^[29,6] ox-LIG exhibits the most intense EPR signal, which may result from greater sparking during laser irradiation. The defects and structural strain in ox-LIG and LIG induced by laser irradiation may benefit electrocatalysis.

2.2. Electrochemical Measurements and Product Analysis

Nitrate reduction was first characterized using an H-cell with Ag/AgCl and platinum foil reference and counter electrodes,

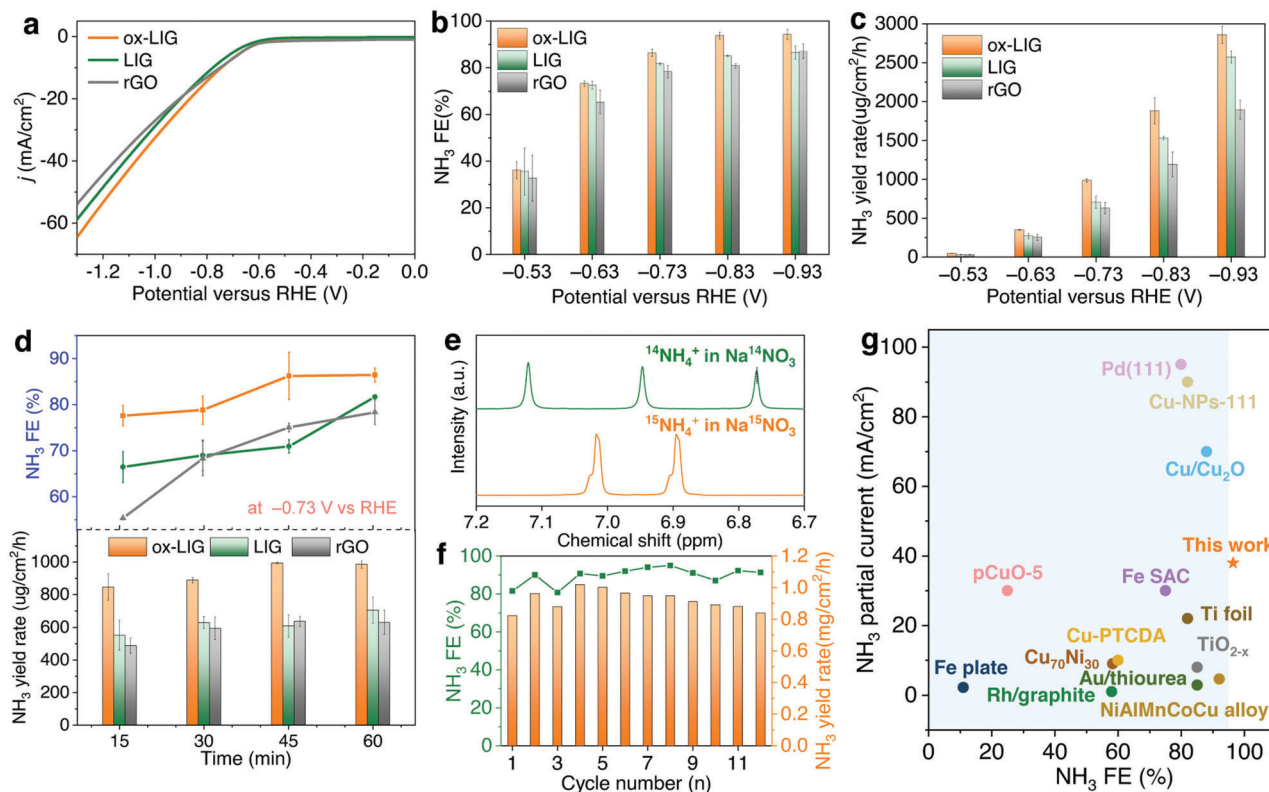


Figure 2. Nitrate reduction performance. a) LSV curves in 1 M NaNO₃ at a scan rate of 10 mV s⁻¹. b) FE of ammonia production and c) ammonia yield rate of ox-LIG, LIG, and rGO. d) Time-dependent FE and yield rate of ammonia at -0.73 V vs RHE. Data are expressed as mean ± SE, n = 3. e) ¹H NMR spectra of ammonia produced from 0.2 M Na¹⁴NO₃ and Na¹⁵NO₃ electrolytes for 1 h. f) ox-LIG stability during cyclic reduction tests at -0.73 V; the cycle time was 0.5 h. g) Partial current density versus FE of NH₃ production at ox-LIG and other electrocatalysts.

respectively. The working electrode was prepared by coating ox-LIG, LIG, or rGO with 1 mg cm⁻² catalyst ink on cellulose paper (CP) sprayed with a layer of Au (Au/CP), as described in the Experimental Section. The supporting electrolyte was 1 M NaNO₃, and all potentials were corrected to the RHE. Optical and SEM images of the surface and cross-section of the catalyst coating on Au/CP are presented in Figures S8 and S9 (Supporting Information). The thickness of the catalyst layer was 70–80 μm. We use Au-coated paper as the current collector because it shows high conductivity and negligible ammonia yield, so that the interference from carbonaceous or metallic electrodes^[13–18] could be minimized. In addition, the large resistivity of rGO or LIGs will cause a significant voltage drop, leading to an underestimated intrinsic performance (Figure S10, Supporting Information). The sheet resistances of catalyst-loaded Au/CP electrodes are collected in Table S2 (Supporting Information). The sheet resistance increases from 12 Ω □⁻¹ for bare Au to 18.8–27 Ω □⁻¹ for the catalyst-loaded electrodes. The electronic conductivity decreases in the sequence LIG > rGO > ox-LIG, which is attributed to the lower oxygen content of LIG and to the fewer defects in rGO relative to ox-LIG. The electrochemical impedance spectroscopy (EIS) measurement in Figure S11 (Supporting Information) presents that the charge transfer resistance at -0.4 V versus RHE of rGO (22.95 ± 0.95 Ω) is larger than ox-LIG (9.95 ± 0.15 Ω) and LIG (13.19 ± 0.21 Ω). At higher overpotential (< -0.6 V), passivated film impedance due to surface polarization becomes significant. Both passivated film impedance

and charge transfer resistance of rGO are the largest at the same overpotential, suggesting its poorest activity toward nitrate reduction.

We have confirmed that NH₃ is produced by the reduction of NO₃⁻. Figure 2a and Figure S12 (Supporting Information) show linear sweep voltammetry (LSV) traces in Na₂SO₄ and NaNO₃ electrolytes. The current density increases with increasing overpotential in the presence of NO₃⁻, which indicates the occurrence of nitrate reduction rather than hydrogen evolution.^[16] The products of nitrate reaction were quantified by colorimetry using the indophenol blue method for NH₃ and the Griess test for NO₂⁻. Ultraviolet–visible (UV–vis) spectroscopy was used to calculate the FE and yields of NH₃ and NO₂⁻. Calibration curves showing the relationship between concentration and UV–vis absorbance are presented in Figures S13 and S14 (Supporting Information). The quantity of NH₃ produced was also determined by ¹H NMR spectroscopy (Figure S16, Supporting Information). The FE of NH₃ production of LIG at -0.73 V detected by the indophenol blue method is 82.4% and 84.8%, respectively. The yield rate established by colorimetry (709.5 μg cm⁻² h⁻¹) is close to that determined by NMR (727 μg cm⁻² h⁻¹), which confirms that nitrate is the source of NH₃. The NH₃ partial current at ox-LIG is much greater than at a bare Au electrode (Figure S17, Supporting Information), which demonstrates the negligible effect of Au/CP on the nitrate reduction reaction.

The FE and production rate of NH₃ are summarized in Figure 2b,c, respectively. NH₃ selectivity at rGO is less than that at

LIG and ox-LIG. ox-LIG attains a FE of $\geq 85\%$ at -0.73 to -0.93 V versus RHE and reaches nearly 100% at -0.93 V. The yield rates of NH_3 at ox-LIG and LIG are greater than at rGO. Furthermore, the ox-LIG attains a yield rate of 150% greater than rGO at high overpotentials. The yield rates of ox-LIG and LIG at -0.93 V are 2859 ± 112.7 and $2572.5 \pm 75.3 \mu\text{g cm}^{-2} \text{h}^{-1}$, respectively. The electrochemical active surface area (ECSA) method is used to normalize the activity of the catalysts.^[3,43–45] As shown in Figures S18 and S19 and Table S3 (Supporting Information), the ECSA of rGO is nearly twice larger than ox-LIG and LIG, while the NH_3 partial current of rGO is twice lower than ox-LIG and LIG after normalization to the ECSA. N_2 adsorption isotherm measurement also suggests a higher specific surface area of rGO (Figure S20, Supporting Information). This indicates the higher performance of LIG and ox-LIG, which is not due to the surface area, but from intrinsically higher catalytic activity.

The electrolysis time also affects selectivity. The NH_3 FEs and yield rates of the three catalysts gradually increase upon prolonging electrolysis from 15 to 60 min (Figure 2d). The NH_3 FE of ox-LIG is surprisingly high at -0.73 V. This parameter reaches 78% after 15 min electrolysis and improves to 86% after 60 min, whereas that of rGO is only 55% after 15 min. The NH_3 FE of ox-LIG is less dependent on reduction time than that of rGO, which indicates more favorable NO_3^- to NH_3 conversion by ox-LIG. The higher hydrophobicity of LIG leads to slightly less nitrate reduction than hydrophilic ox-LIG, but LIG is still superior to rGO in this respect. The nitrate reduction reaction of the commercial amorphous carbon materials—carbon black (CB) is studied for comparison.^[46,47] The absence of 2D peak in the Raman spectrum of CB (Figure S21a, Supporting Information) reveals that CB adopts a different structure from LIG.^[30,47] Figure S21c,d (Supporting Information) shows that the NH_3 FE and yield rate of CB are significantly lower than those of graphene materials, suggesting that both amorphous atomic structure and graphene feature contribute to the catalytic activity. The nitrate-to-ammonia conversion efficiency of ox-LIG at -0.83 V in the electrolytes with concentrations of 0.2, 0.4, 0.6, 0.8, and 1 M are investigated and presented in Figure S22 (Supporting Information). The NH_3 partial current density correlates with the nitrate concentration (Figure S23, Supporting Information).

Isotope labeling experiments by electrolyzing $\text{Na}^{14}\text{NO}_3$ and $\text{Na}^{15}\text{NO}_3$ solutions (Figure 2e) were conducted to verify the source of NH_3 formation. ^1H NMR coupled with UV–vis absorption was used to determine the NH_3 produced. Three peaks for $^{14}\text{NH}_4^+$ at $\delta = 7.12, 6.94,$ and 6.77 ppm are observed when $\text{Na}^{14}\text{NO}_3$ is used as the electrolyte. However, only two peaks corresponding to $^{15}\text{NH}_4^+$ at $\delta = 7.01$ and 6.89 ppm are found upon the electroreduction of $\text{Na}^{15}\text{NO}_3$. Quantification of ammonia using UV–vis method shows NH_3 FE of 46% and 40% for electroreduced 0.2 M $\text{Na}^{14}\text{NO}_3$ and $\text{Na}^{15}\text{NO}_3$, respectively. This result confirms that ammonia is produced solely via nitrate reduction.

Figure 2f shows the results of cycling tests using ox-LIG for NO_3^- at -0.73 V. The FE and yield rate of NH_3 remain unchanged after 12 consecutive cycles, indicating the superior stability of the catalyst. Figure 2g compares the nitrate reduction performance of ox-LIG with that of other electrocatalysts, and the detailed comparison of nitrate reduction performance is summarized in Table S4 (Supporting Information). It should be noted that the test conditions in the literature are different. Thus, the comparison

might not be fully conclusive. Nonetheless, ox-LIG exhibits a high FE for NH_3 production at high partial current densities that is superior or comparable to the performance of non-noble metal or alloy catalysts (Fe, Ti, CuNi)^[12,17,48–50] and noble metal (Au in this work and $\text{Rh}^{[51]}$) catalysts.

Nitrite ion is a minor product of NO_3^- reduction. The FE of NO_2^- production is summarized in Figure S24 (Supporting Information). The FE of NO_2^- formation decreases with increasing overpotential, which is contrary to the behavior of NH_3 . Figure S25 (Supporting Information) shows that the NO_2^- FE at -0.73 V remains nearly constant from 15 to 60 min for all three catalysts, which differs from the FE behavior of NH_3 (Figure 2d). Prolonging the electrolysis time increases the concentration of NO_2^- , which can serve as an additional nitrogen source for ammonia electrosynthesis.

To rule out the possible interference of metal impurities, we first measured the metal contents in electrolyte and catalysts by inductively coupled plasma-optical emission spectroscopy (ICP-OES). As shown in Table S5 (Supporting Information), there are no active metal impurities in electrolyte and ox-LIG and LIG. However, 0.73 mg g^{-1} of Fe is found in rGO due to the massive chemical use in the sophisticated preparation process.^[53] To further rule out the possible contaminations from the reference electrode and the platinum counter electrode, a control experiment at a constant current density of 15 mA cm^{-2} with carbon paper as the counter electrode and without reference electrode was performed (Figure S26, Supporting Information). The performance is consistent with the yield rate and selectivity of ox-LIG using the three-electrode configuration (Figure 2b,c and Figure S15 (Supporting Information)).

In situ FTIR spectroscopy^[54] was used to provide insight into the mechanism of nitrate reduction and the detection of adsorbed reaction intermediates. Potential-dependent transmittance spectra of ox-LIG and rGO are presented in Figure 3a. The peak at $\approx 1633 \text{ cm}^{-1}$ is attributed to the O–H bending of water.^[54,55] This signal is more significant for ox-LIG at higher overpotentials, possibly due to the enhanced adsorption of water^[55] and the formation of hydroxide from electroreduction. The new band at 1242 cm^{-1} indicates the formation of NO_2^- .^[54] The peaks at 1444, 1294, and 1116 cm^{-1} at -1 V of ox-LIG are assigned to molecularly adsorbed NH_3 .^[55–57] These peaks shift to 1442, 1292, and 1109 cm^{-1} at -0.8 V, respectively, possibly due to the change of adsorption configuration under varied potentials.^[55,58] The peak at $1350\text{--}1380 \text{ cm}^{-1}$ merges at high overpotential in both ox-LIG and rGO, assigned to NO_3^- possibly due to the change of local concentration due to highly polarized surface.^[52,59] For control sample of Au-coated prism, only O–H bending at $\approx 1633 \text{ cm}^{-1}$ and nitrate signal at $1350\text{--}1380 \text{ cm}^{-1}$ can be found (Figure S27, Supporting Information), which is consistent with the poor nitrate reduction of Au (Figure S17, Supporting Information). The in situ FTIR spectra tested in 1 M NaCl are shown in Figure 3b. The reducing potential induces negligible fluctuation of the peak intensities. It confirms that the increase of peaks in $1116\text{--}1444 \text{ cm}^{-1}$ in FTIR spectra in NaNO_3 (Figure 3a) results from the nitrogen species rather than the oxygen species in the graphenic materials. The NH_3 band on ox-LIG, which emerges at 0 V, is enhanced at greater overpotentials. By contrast, rGO generates a very weak NH_3 band only at high overpotentials. This suggests that ox-LIG has a smaller onset overpotential and greater NH_3

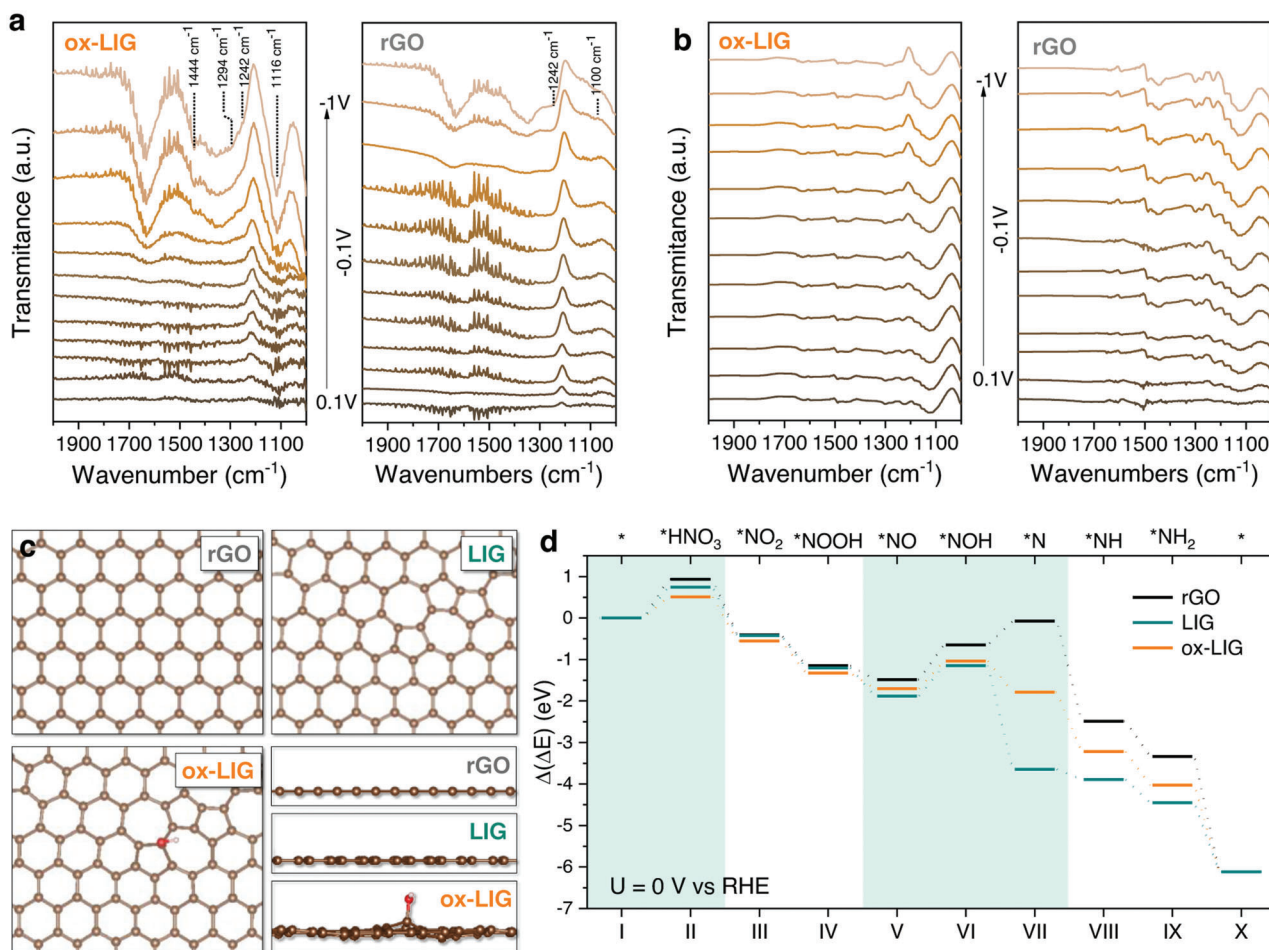


Figure 3. In situ FTIR spectra and theoretical calculations. a,b) Potential-dependent transmittance spectra of ox-LIG and rGO in 1 M NaNO₃ (a) and 1 M NaCl (b). The reference spectrum was recorded at +0.2 V vs RHE. c) DFT-calculated models of LIG, ox-LIG, and rGO. The red, brown, and pink spheres represent oxygen, carbon, and hydrogen, respectively. d) Free energy diagrams of complete NO₃⁻ to NH₃ conversion on LIG, ox-LIG, and rGO.

yield than rGO. The nitrite band on rGO is more intense than that on ox-LIG, which agrees with the greater NO₂⁻ FE of rGO (Figure S24, Supporting Information). The in situ FTIR spectra confirm the greater catalytic activity of ox-LIG for the reduction of nitrate.

2.3. Theoretical Calculations

We performed DFT calculations of reaction pathways^[7,60] to understand the origin of the high NH₃ selectivity. Our experimental data suggest that both ox-LIG and LIG with amorphous lattice show higher activity than higher-crystallinity rGO, and ox-LIG is more active than LIG. Thus, here we mainly focus on the activity of amorphous carbon and the effect of oxygen; it does not rule out the possible contribution from the nitrogen of LIGs, whose content is only 1–2% (Table S1, Supporting Information). The three models of graphene are shown in Figure 3c. One model comprises five-, six-, and seven-membered rings to represent the amorphous nature of LIG. A hydroxyl group is fixed at the surface of LIG to represent the local structure of ox-LIG. The other model comprises only six-membered rings to represent rGO. Fig-

ure 3d shows the change in adsorption energy of all possible intermediates during nitrate reduction. We first compare the activity of rGO and LIG. There are two energies unfavorable steps, which are the adsorption of NO₂OH and the transition of *NO → *NOH. Both energy barriers are smaller for LIG. The reduction of *NO to *NOH has been reported as a key step for some catalysts in producing NH₃.^[7,61,62] *NO to *NOH conversion is an uphill process for rGO (+0.84 eV), whereas this energy is reduced to +0.66 eV for ox-LIG. *NOH is ultimately reduced to *N followed by hydrogenation to yield *NH, *NH₂, and NH₃. The conversion of *NOH to *N remains unfavorable for rGO, but it becomes a downhill process for LIG. We further compare the energies of ox-LIG and LIG (Figure 3d) to understand the effect of the hydroxide group in catalyzing nitrate-to-ammonia conversion. In general, their energy barriers are more favorable than rGO. The adsorption of NO₂OH on ox-LIG is lower than LIG by 0.24 eV. Early studies suggested that the hydroxide group could stabilize the adsorption of *NO_x species by hydrogen bonds.^[63] We observed a hydrogen bond distance of 2.97 and 2.55 Å for *NO₂OH and *NO₂ on ox-LIG, respectively, which agrees with the literature.^[63] To conclude, we attribute the enhanced activities of LIG and ox-LIG to the amorphous structure that can undergo

structural deformation to stabilize the adsorbed species, whereas rGO has lower activity due to its aromaticity. The existence of hydrogen bonds in ox-LIG further improves the reaction pathway.

2.4. Agricultural Applications

Herein, we demonstrate that electrochemically reduced nitrate can be used to promote the growth of plants in recognition of the fact that ammonia is a potent chemical for increasing crop yields.^[64,65] Figure 4a contains a schematic for the remediation of nitrate-polluted water to close the NO_x cycle. Nitrate from polluted groundwater and industrial wastewater is electroreduced to NH₃ after purification and concentration and then reused as a fertilizer for vegetable growth or as a fuel. The influence of NaNO₃ on vegetable growth before and after electrolysis is also explored.

Because ox-LIG can produce large quantities of NH₃ at high current densities, we first demonstrate the use of the flow electrolyzer for the on-demand synthesis and controlled release of ammonia.^[68] The flow cell (Figure S29, Supporting Information), which uses peristaltic pumps to improve mass transport,^[67,68] can produce massive amounts of ammonia at large and stable currents (Figure 4b). Figure 4c summarizes the nitrate reduction performance of ox-LIG using the flow cell. The NH₃ FE reaches 72% at a current density of 200 mA cm⁻² and flow rate of 0.5 mL min⁻¹. Movie S1 (Supporting Information) shows the feasibility of instant ammonia acquisition from nitrate reduction. Cabbages and radishes are then cultivated using the electroreduced NaNO₃ as fertilizer. The pH of the electrolysis product is neutralized with atmospheric CO₂ before irrigation. Figure 4d,f and Figures S30–S32 (Supporting Information) show that the two vegetables flourish more productively when cultivated with reduced electrolyte than with NaNO₃. The statistical results in Figure 4e,g show that the electroreduced material significantly promotes vegetable growth and stimulates crop yield by more than 200% relative to NaNO₃. The survival rate also improves by 30% for cabbage and 86% for radish. The incorporation of trace elements and optimization of the NH₃ concentration from the flow electrolyzer may further improve crop yields. These practical applications show that ammonia from electroreduced nitrate is conducive to vegetable growth and offers an effective means of closing the NO_x cycle.

3. Conclusions

Ammonia plays an essential role in the agricultural and pharmaceutical industries.^[71] This study describes the first example of NO₃⁻-to-NH₃ reduction by a nonmetallic catalyst with an activity comparable to that of state-of-the-art metallic catalysts. HRTEM imaging, PDF analysis, in situ FTIR spectroscopy, and DFT calculations reveal the unique atomic features of amorphous graphene that facilitate the adsorption of intermediates and formation of NH₃ during NO₃⁻ reduction. The elevated NH₃ selectivity of amorphous graphene also enables the construction of a flow electrolyzer coupled with an in situ sensing platform^[70] to create a smart agricultural system based on electrolytically produced ammonia.^[66,71] Controlled release of ammonia can be achieved by using direct laser-writing techniques to fabricate

graphene-based sensors and in situ detection modules. Our results will stimulate the design and development of nonmetal electrocatalysts for nitrate reduction with important implications for wastewater remediation.

4. Experimental Section

Fabrication of LIG: A 120 μm-thick polyimide (PI) film was irradiated with a 10.6 μm CO₂ laser marking machine (Minsheng Laser #MSDB-FM60 CO₂ Laser Marker, 60 W) in ambient and N₂ atmospheres to fabricate ox-LIG and LIG, respectively. The laser power, speed, pulses per dot, and line spacing were set at 1.8 W, 1000 mm s⁻¹, 5, and 0.03 mm, respectively. The laser was operated in the vector mode. LIG powder was scraped from the PI film and collected for catalyst fabrication.

Fabrication of rGO: GO was prepared by a modified Hummers' method.^[26–28] rGO was prepared by annealing GO under Ar at 1000 °C in a tube furnace. The GO color changed from brown to black upon reduction.

Catalyst Synthesis and Working Electrode Preparation: Gold was sputtered onto tailored CP (area = 1 cm²) with a sputter coater (SCD 050). The current and spraying time were set at 60 mA and 120 s, respectively. The resulting Au/CP film, which was used as catalyst support, exhibited enhanced tenacity and conductivity. CB (Vulcan XC-72) powders were purchased from Fuel Cell Store, USA. 5 mg of catalyst (ox-LIG, LIG, rGO, or CB) and 500 μL Nafion solution (Sigma-Aldrich, 5 wt% Nafion 117) were mixed and sonicated for 30 min. The homogenous catalyst ink was gently dropped onto the Au/CP at 1 mg cm⁻² loading and dried at room temperature.

General Characterization: SEM and TEM images were collected with QUANTRO S and Themis Z microscopes, respectively, from Thermo Fisher. Contact angles were measured with a Ramé-Hart Model 190 goniometer. Raman spectra were obtained at 514 nm with a LabRAM HR800 confocal laser micro-Raman spectrometer. UV–visible spectra were obtained by use of a Shimadzu 1700 spectrophotometer. XRD patterns were obtained with a SmartLab diffractometer. XPS spectra were collected with a Thermo ESCALAB 250Xi spectrometer. NH₃ quantification and isotope tracking were conducted by ¹H NMR spectroscopy at 600 MHz with a Bruker spectrometer ASCEND AVANCE III HD. EPR spectra were obtained by an ADANI SPINSCA X spectrometer at room temperature. In situ FTIR spectra were obtained with a Perkin-Elmer Spectrum 100 instrument. The purities of electrolyte and catalysts were measured via an ICP-OES Optima 8000 spectrometer. PDF analysis was extracted from high-energy synchrotron X-ray total scattering by direct Fourier transform of the reduced structure function $[F(Q)]$, up to $Q \approx 24.7 \text{ \AA}^{-1}$ using the 11-ID-C beamline at Advanced Photon Source (APS) of Argonne National Lab (ANL) (X-ray wavelength = 0.1173 Å). The $G(r)$ functions, $G(r) = 4\pi[\rho(r) - \rho_0]$, where $\rho(r)$ and ρ_0 are the local and average atomic number densities, were computed with PDFgetX3 software.

Electrochemical Measurements: Electrochemical nitrate reduction was carried out in a three-compartment H-cell. The cathode and anode compartments were separated by a Nafion-117 membrane (Fuel Cell Store). Platinum foil and a LF-2 Ag/AgCl electrode (calibrated before use) were used as the counter and reference electrodes, respectively. LSV was conducted from 0 to -1.3 V versus RHE in 1 M NaNO₃ at a scan rate of 10 mV s⁻¹. All potentials were referenced to the RHE by the following equation

$$E \text{ vs RHE} = E \text{ vs Ag/AgCl} + 0.23 + 0.0592 \times \text{pH} \quad (1)$$

The cell was purged with high-purity Ar at a flow rate of 10 cm³ min⁻¹ during electrochemical measurements. The exiting Ar gas was collected in dilute HCl solution. Electrochemical experiments were carried out with a CHI 760E potentiostat employing 95% resistance compensation. Electrolytes in the flow-cell electrolyzer were purged with Ar gas for 0.5 h before experiments and were circulated through the working and counter electrode compartments using peristaltic pumps (Longer, BT100-2) operating at 0.5 mL min⁻¹.

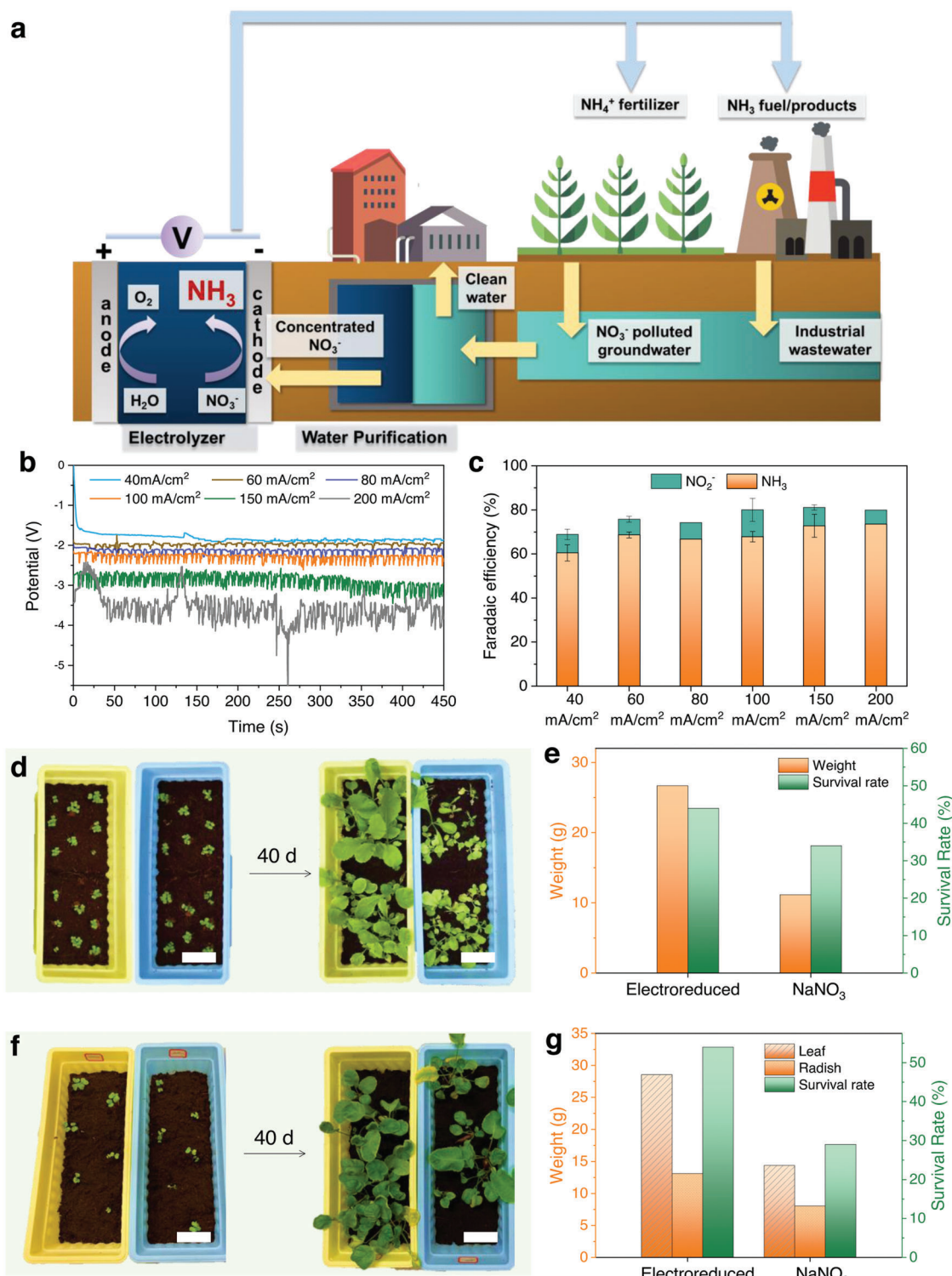


Figure 4. Practical application of the flow-cell electrolyzer. a) Schematic cycle of ammonia synthesis from waste nitrate. b) Chronopotentiometry at varied current densities and c) NH₃ FE of ox-LIG as a function of current density in a flow-cell electrolyzer with 1 M NaNO₃. Data are expressed as mean ± SE, *n* = 3. d, f) Digital photos of cabbage (d) and radishes (f) growth. Scale bars: 10 cm. The blue pots were cultivated with the as-prepared NaNO₃; the yellow pots were cultivated with electroreduced NaNO₃. e, g) Statistics of cabbage (e) and radish (g) growth in terms of leaf weight, fruit weight, and survival rate.

Theoretical Calculations: Spin-polarized DFT calculations were performed using the plane-wave basis Vienna ab initio simulation package code.^[28,72] The generalized gradient approximation in the Perdew–Burke–Ernzerhof formulation was used with a cutoff energy of 600 eV. An $\approx 18 \text{ \AA}$ vacuum space was added as interlamination to eliminate interaction between layers. For reactions involving the transfer of a H^+/e^- pair, the free energy of the pair was set to one-half the free energy of gaseous H_2 ($\text{H}^+ + \text{e}^- \leftrightarrow \frac{1}{2}\text{H}_2$).^[75] The binding energies of nitrate were corrected with a gas-phase reference based on HNO_3 .^[7,74] The Gibbs free energy changes ($\Delta\Delta G$) were calculated using the computational hydrogen electrode model and defined as^[75,76]

$$\Delta\Delta G = \Delta E_b + \Delta\text{ZPE} - T\Delta S \quad (2)$$

where ΔE_b is the reaction energy, and ΔZPE and $T\Delta S$ are changes in the zero-point energy and entropy of a species, respectively. The reaction energy was calculated as

$$\Delta E_b = E_{\text{tot}} - E_{\text{molecular}} - E_{\text{adsorbate}} \quad (3)$$

where E_{tot} , $E_{\text{molecular}}$, and $E_{\text{adsorbate}}$ are the total energy of molecular with adsorbate, the energy of clean molecular, and the energy of adsorbate in the gas phase, respectively.

Product Analysis: The quantities of NH_3 and NO_2^- in the electrolyte were determined by colorimetry using the indophenol blue method and the Griess test, respectively.^[1,77] Two reagents were prepared for NH_3 calibration. Reagent A comprised 2 mL of 1 M NaOH solution containing 5 wt% salicylic acid and 5 wt% sodium citrate. Reagent B was prepared by mixing 1 mL 0.05 M NaClO and 0.2 mL 1 wt% sodium nitroferrocyanide. Reagents A and B were added to 2 mL NH_4NO_3 solution with concentrations of 0.1, 0.2, 0.3, 0.4, and 0.5 mM. The absorbance at 650 nm was recorded by UV–vis spectrophotometry after a 2 h incubation period. The quantity of NH_3 produced was determined from the amount of indophenol blue formed from 2 mL electrolyte, 2 mL reagent A, and 1 mL reagent B. NO_2^- calibration was based on the reaction of the Griess reagent and NaNO_2 at concentrations of 0.05, 0.1, 0.2, 0.3, and 0.4 mM. The Griess reagent was prepared by dissolving 0.1 g *N*-(1-naphthyl)ethylenediamine dihydrochloride, 1 g sulfonamide, and 2.94 mL H_3PO_4 in 50 mL deionized (DI) water. The Griess reagent, electrolyte, and DI water were mixed in a 1:1:2 volume ratio and allowed to stand for 15 min. The absorbance at 540 nm was used to determine the concentration of NO_2^- . Dilution of the electrolyte prior to UV–vis measurement was needed when NH_3 and NO_2^- concentrations in the electrolyte were high. Quantification of ammonia was confirmed by ^1H NMR spectroscopy using benzoic acid as an internal standard. The Faradaic efficiencies of NH_3 and NO_2^- were calculated as follows

$$\text{NH}_3 \text{ Faradaic efficiency} = \frac{(8 \times F \times C(\text{NH}_3) \times V)}{Q} \quad (4)$$

$$\text{NO}_2^- \text{ Faradaic efficiency} = \frac{(2 \times F \times C(\text{NO}_2^-) \times V)}{Q} \quad (5)$$

where F is the Faraday constant, $C(\text{NH}_3)$ and $C(\text{NO}_2^-)$ are the molar concentrations of NH_3 and NO_2^- , V is the electrolyte volume, and Q is the charge (in Coulombs) passing through the catalyst.

Isotope Labeling Experiments: 0.2 M $\text{Na}^{15}\text{NO}_3$ was used as the electrolyte in isotope labeling experiments. $^{15}\text{NH}_4^+$ was measured by NMR spectroscopy at 600 MHz after 1 h electroreduction to establish the nitrogen source of NH_3 produced by electrolysis.

Plant Growth: Equal quantities of cabbage and radish seeds were sowed in rows in culturing pots. The control groups were watered with 5 mM NaNO_3 . The test groups were watered with electrolyte produced by electroreduction of 1 M NaNO_3 in a flow cell operating at 0.5 mL min^{-1} . The electrolyte was diluted 200-fold after reduction, and CO_2 gas was purged through the solution to adjust the pH to ≈ 7 . The crop yield was weighed, and the number of viable plants was recorded after 40 days.

Statistical Analysis: Data for FE calculation were expressed as mean \pm standard error (SE), $n = 3$. 16 zones with seeds from the same source were selected for plant growth. Dead plants were not included in the crop yield calculation.

Supporting Information

Supporting Information is available from the Wiley Online Library or from the author.

Acknowledgements

The study described in this paper was partially supported by the Shenzhen Science and Technology Program (JCYJ20220818101204009), the Young Scientists Fund of the National Natural Science Foundation of China (Project No. 21905240) and the State Key Laboratory of Marine Pollution Seed Collaborative Research Fund (Grant No. SKLMP/IRF/0029). R.Y. also acknowledges the support from the Chow Sang Sang Group Research Fund (Project No. 9229060) sponsored by the Chow Sang Sang Holdings International Limited and CityU Applied Research Grant (Project No. 9667224). This research used resources of the Advanced Photon Source, a U.S. Department of Energy (DOE) Office of Science User Facility, operated for the DOE Office of Science by the Argonne National Laboratory under Contract No. DE-AC02-06CH11357. Computational modeling work at Rice (J.-J.Z. and B.I.Y.) was supported by the Office of Naval Research (N00014-22-1-2788).

Conflict of Interest

The authors declare no conflict of interest.

Author Contributions

R.Y. designed the experiment. L.H. conducted the LIG synthesis and characterization. H.Z., Q.L., and Y.R. collected the PDF data. J.-J.Z. and B.I.Y. performed the theoretical calculations. M.Z. conducted the FTIR study. L.H. and R.Y. wrote the paper with comments from other authors. R.Y. provided regular supervision and oversaw the research.

Data Availability Statement

The data that support the findings of this study are available from the corresponding author upon reasonable request.

Keywords

ammonia synthesis, amorphous graphene, laser induction, nitrate reduction, wastewater remediation

Received: December 18, 2022
Revised: February 12, 2023
Published online: April 28, 2023

- [1] G. F. Chen, Y. Yuan, H. Jiang, S. Y. Ren, L. X. Ding, L. Ma, T. Wu, J. Lu, H. Wang, *Nat. Energy* **2020**, *5*, 605.
- [2] C. Zamfirescu, I. Dincer, *J. Power Sources* **2008**, *185*, 459.
- [3] Y. Wang, W. Zhou, R. Jia, Y. Yu, B. Zhang, *Angew. Chem.* **2020**, *132*, 5388.

- [4] J. Li, G. Zhan, J. Yang, F. Quan, C. Mao, Y. Liu, B. Wang, F. Lei, L. Li, A. W. M. Chan, L. Xu, Y. Shi, Y. Du, W. Hao, P. K. Wong, J. Wang, S. X. Dou, L. Zhang, J. C. Yu, *J. Am. Chem. Soc.* **2020**, *142*, 7036.
- [5] F. Jiao, B. Xu, *Adv. Mater.* **2019**, *31*, 1805173.
- [6] R. Daiyan, T. Tran-Phu, P. Kumar, K. Iputera, Z. Tong, J. Leverett, M. H. A. Khan, A. A. Esmailpour, A. Jalili, M. Lim, A. Tricoli, R.-S. Liu, X. Lu, E. Lovell, R. Amal, *Energy Environ. Sci.* **2021**, *14*, 3588.
- [7] Z.-Y. Wu, M. Karamad, X. Yong, Q. Huang, D. A. Cullen, P. Zhu, C. Xia, Q. Xiao, M. Shakouri, F.-Y. Chen, J. Y. Kim, Y. Xia, K. Heck, Y. Hu, M. S. Wong, Q. Li, I. Gates, S. Siahrostami, H. Wang, *Nat. Commun.* **2021**, *12*, 2870.
- [8] P. H. van Langevelde, I. Katsounaros, M. T. M. Koper, *Joule* **2021**, *5*, 290.
- [9] Y. Ren, C. Yu, L. Wang, X. Tan, Z. Wang, Q. Wei, Y. Zhang, J. Qiu, *J. Am. Chem. Soc.* **2022**, *144*, 10193.
- [10] L. Li, C. Tang, X. Cui, Y. Zheng, X. Wang, H. Xu, S. Zhang, T. Shao, K. Davey, S.-Z. Qiao, *Angew. Chem., Int. Ed.* **2021**, *60*, 14131.
- [11] J. Sun, D. Alam, R. Daiyan, H. Masood, T. Zhang, R. Zhou, P. J. Cullen, E. C. Lovell, A. (Rouhollah) Jalili, R. Amal, *Energy Environ. Sci.* **2021**, *14*, 865.
- [12] J. M. McEnaney, S. J. Blair, A. C. Nielander, J. A. Schwalbe, D. M. Koshy, M. Cargnello, T. F. Jaramillo, *ACS Sustainable Chem. Eng.* **2020**, *8*, 2672.
- [13] J. Martínez, A. Ortiz, I. Ortiz, *Appl. Catal., B* **2017**, *207*, 42.
- [14] S. Garcia-Segura, M. Lanzarini-Lopes, K. Hristovski, P. Westerhoff, *Appl. Catal., B* **2018**, *236*, 546.
- [15] W. Teng, N. Bai, Y. Liu, Y. Liu, J. Fan, W. X. Zhang, *Environ. Sci. Technol.* **2018**, *52*, 230.
- [16] W. Duan, G. Li, Z. Lei, T. Zhu, Y. Xue, C. Wei, C. Feng, *Water Res.* **2019**, *161*, 126.
- [17] R. Jia, Y. Wang, C. Wang, Y. Ling, Y. Yu, B. Zhang, *ACS Catal.* **2020**, *10*, 3533.
- [18] Y. Wang, A. Xu, Z. Wang, L. Huang, J. Li, F. Li, J. Wicks, M. Luo, D. H. Nam, C. S. Tan, Y. Ding, J. Wu, Y. Lum, C. T. Dinh, D. Sinton, G. Zheng, E. H. Sargent, *J. Am. Chem. Soc.* **2020**, *142*, 5702.
- [19] J. Ding, W. Li, Q.-L. Zhao, K. Wang, Z. Zheng, Y.-Z. Gao, *Chem. Eng. J.* **2015**, *271*, 252.
- [20] X. Rao, X. Shao, J. Xu, J. Yi, J. Qiao, Q. Li, H. Wang, M. Chien, C. Inoue, Y. Liu, J. Zhang, *Sep. Purif. Technol.* **2019**, *216*, 158.
- [21] W. Zhu, X. Zhang, Y. Yin, Y. Qin, J. Zhang, Q. Wang, *Electrochim. Acta* **2018**, *291*, 328.
- [22] M. Ghazouani, H. Akrouf, L. Bousselemi, *Desalin. Water Treat.* **2015**, *53*, 1107.
- [23] M. Ghazouani, H. Akrouf, L. Bousselemi, *Environ. Sci. Pollut. Res.* **2017**, *24*, 9895.
- [24] J. Lin, Z. Peng, Y. Liu, F. Ruiz-Zepeda, R. Ye, E. L. G. Samuel, M. J. Yacaman, B. I. Jakobson, J. M. Tour, *Nat. Commun.* **2014**, *5*, 5714.
- [25] R. W. Dreyfus, *Appl. Phys. A* **1992**, *55*, 335.
- [26] G. Eda, G. Fanchini, M. Chhowalla, *Nat. Nanotechnol.* **2008**, *3*, 270.
- [27] M. Hirata, T. Gotou, S. Horiuchi, M. Fujiwara, M. Ohba, *Carbon* **2004**, *42*, 2929.
- [28] S. Stankovich, D. A. Dikin, R. D. Piner, K. A. Kohlhaas, A. Kleinhammes, Y. Jia, Y. Wu, S. T. Nguyen, R. S. Ruoff, *Carbon* **2007**, *45*, 1558.
- [29] B. Wang, V. Likodimos, A. J. Fielding, R. A. W. Dryfe, *Carbon* **2020**, *160*, 236.
- [30] A. C. Ferrari, J. C. Meyer, V. Scardaci, C. Casiraghi, M. Lazzeri, F. Mauri, S. Piscanec, D. Jiang, K. S. Novoselov, S. Roth, A. K. Geim, *Phys. Rev. Lett.* **2006**, *97*, 187401.
- [31] A. Gupta, G. Chen, P. Joshi, S. Tadigadapa, P. C. Eklund, *Nano Lett.* **2006**, *6*, 2667.
- [32] I. Calizo, I. Bejenari, M. Rahman, G. Liu, A. A. Balandin, *J. Appl. Phys.* **2009**, *106*, 043509.
- [33] Y. Gong, D. Li, Q. Fu, C. Pan, *Prog. Nat. Sci.: Mater. Int.* **2015**, *25*, 379.
- [34] B. Govindan, S. Anwer, M. R. Viswanathan, E. Alhseinat, F. Banat, P. Nagamony, *Sci. Rep.* **2018**, *8*, 5718.
- [35] M. Mohandoss, S. Sen Gupta, A. Nelleri, T. Pradeep, S. M. Maliyekkal, *RSC Adv.* **2017**, *7*, 957.
- [36] M. S. A. Sher Shah, A. R. Park, Z. Kan, J. H. Park, P. J. Yoo, *ACS Appl. Mater. Interfaces* **2012**, *4*, 3893.
- [37] L. Huang, S. Xu, Z. Wang, K. Xue, J. Su, Y. Song, S. Chen, C. Zhu, B. Z. Tang, R. Ye, *ACS Nano* **2020**, *14*, 12045.
- [38] X. Jiao, Y. Qiu, L. Zhang, X. Zhang, *RSC Adv.* **2017**, *7*, 52337.
- [39] I. O. Faniyi, O. Fasakin, B. Olofinjana, A. S. Adekunle, T. V. Oluwasusi, M. A. Eleruja, E. O. B. Ajayi, *SN Appl. Sci.* **2019**, *1*, 1181.
- [40] D. Luo, D. Hui, B. Wen, R. Li, J. Yang, X. Shen, A. H. Reid, S. Weathersby, M. E. Kozina, S. Park, Y. Ren, T. D. Loeffler, S. K. R. S. Sankaranarayanan, M. K. Y. Chan, X. Wang, J. Tian, I. Arslan, X. Wang, T. Rajh, J. Wen, *Phys. Rev. B* **2020**, *102*, 155431.
- [41] A. Burian, J. C. Dore, K. Jurkiewicz, *Rep. Prog. Phys.* **2018**, *82*, 016501.
- [42] N. Woznica, L. Hawelek, H. E. Fischer, I. Bobrinetskiy, A. Burian, *J. Appl. Crystallogr.* **2015**, *48*, 1429.
- [43] R. Ye, P. del Angel-Vicente, Y. Liu, M. J. Arellano-Jimenez, Z. Peng, T. Wang, Y. Li, B. I. Jakobson, S.-H. Wei, M. J. Yacaman, J. M. Tour, *Adv. Mater.* **2016**, *28*, 1427.
- [44] J. Kibsgaard, T. F. Jaramillo, *Angew. Chem., Int. Ed.* **2014**, *53*, 14433.
- [45] E. J. Popczun, J. R. McKone, C. G. Read, A. J. Bicchieri, A. M. Wiltrout, N. S. Lewis, R. E. Schaak, *J. Am. Chem. Soc.* **2013**, *135*, 9267.
- [46] A. Ambrosi, M. Pumera, *J. Phys. Chem. C* **2011**, *115*, 25281.
- [47] C. H. An Wong, A. Ambrosi, M. Pumera, *Nanoscale* **2012**, *4*, 4972.
- [48] L. Mattarozzi, S. Cattarin, N. Comisso, A. Gambirasi, P. Guerriero, M. Musiani, L. Vázquez-Gómez, E. Verlato, *Electrochim. Acta* **2014**, *140*, 337.
- [49] M. Li, C. Feng, Z. Zhang, N. Sugiura, *Electrochim. Acta* **2009**, *54*, 4600.
- [50] C. Lu, S. Lu, W. Qiu, Q. Liu, *Electrochim. Acta* **1999**, *44*, 2193.
- [51] O. Brylev, M. Sarrazin, L. Roué, D. Bélanger, *Electrochim. Acta* **2007**, *52*, 6237.
- [52] R. Ye, J. Dong, L. Wang, R. Mendoza-Cruz, Y. Li, P.-F. An, M. J. Yacaman, B. I. Jakobson, D. Chen, J. M. Tour, *Carbon* **2018**, *132*, 623.
- [53] Y. Wang, C. Wang, M. Li, Y. Yu, B. Zhang, *Chem. Soc. Rev.* **2021**, *50*, 6720.
- [54] E. Pérez-Gallent, M. C. Figueiredo, I. Katsounaros, M. T. M. Koper, *Electrochim. Acta* **2017**, *227*, 77.
- [55] Y. Yao, S. Zhu, H. Wang, H. Li, M. Shao, *J. Am. Chem. Soc.* **2018**, *140*, 1496.
- [56] H. Li, J. Shang, Z. Ai, L. Zhang, *J. Am. Chem. Soc.* **2015**, *137*, 6393.
- [57] Y. Yao, S. Zhu, H. Wang, H. Li, M. Shao, *Angew. Chem.* **2020**, *132*, 10565.
- [58] S. Zhu, X. Qin, F. Xiao, S. Yang, Y. Xu, Z. Tan, J. Li, J. Yan, Q. Chen, M. Chen, M. Shao, *Nat. Catal.* **2021**, *4*, 711.
- [59] M. C. P. M. da Cunha, J. P. I. De Souza, F. C. Nart, *Langmuir* **2000**, *16*, 771.
- [60] L. Cheng, T. Ma, B. Zhang, L. Huang, W. Guo, F. Hu, H. Zhu, Z. Wang, T. Zheng, D.-T. Yang, C.-K. Siu, Q. Liu, Y. Ren, C. Xia, B. Z. Tang, R. Ye, *ACS Catal.* **2022**, *12*, 11639.
- [61] H. Shin, S. Jung, S. Bae, W. Lee, H. Kim, *Environ. Sci. Technol.* **2014**, *48*, 12768.
- [62] H.-J. Chun, V. Apaja, A. Clayborne, K. Honkala, J. Greeley, *ACS Catal.* **2017**, *7*, 3869.
- [63] S. Tang, Z. Cao, *J. Chem. Phys.* **2011**, *134*, 044710.
- [64] D. Tilman, K. G. Cassman, P. A. Matson, R. Naylor, S. Polasky, *Nature* **2002**, *418*, 671.
- [65] C. Liu, K. K. Sakimoto, B. C. Colón, P. A. Silver, D. G. Nocera, *Proc. Natl. Acad. Sci. USA* **2017**, *114*, 6450.
- [66] T. N. Q. Le, N. N. Tran, M. Escribá-Gelonch, C. A. Serra, I. Fisk, D. J. McClements, V. Hessel, *Chem. Soc. Rev.* **2021**, *50*, 11979.

- [67] Y. Song, J.-J. Zhang, Y. Dou, Z. Zhu, J. Su, L. Huang, W. Guo, X. Cao, L. Cheng, Z. Zhu, Z. Zhang, X. Zhong, D. Yang, Z. Wang, B. Z. Tang, B. I. Yakobson, R. Ye, *Adv. Mater.* **2022**, *34*, 2110496.
- [68] J. Su, J.-J. Zhang, J. Chen, Y. Song, L. Huang, M. Zhu, B. I. Yakobson, B. Z. Tang, R. Ye, *Energy Environ. Sci.* **2021**, *14*, 483.
- [69] L. Hollevoet, F. Jardali, Y. Gorbanev, J. Creel, A. Bogaerts, J. A. Martens, *Angew. Chem., Int. Ed.* **2020**, *59*, 23825.
- [70] L. Huang, J. Su, Y. Song, R. Ye, *Nano-Micro Lett.* **2020**, *12*, 157.
- [71] H. Yin, Y. Cao, B. Marelli, X. Zeng, A. J. Mason, C. Cao, *Adv. Mater.* **2021**, *33*, 2007764.
- [72] G. Kresse, D. Joubert, *Phys. Rev. B* **1999**, *59*, 1758.
- [73] A. A. Peterson, F. Abild-Pedersen, F. Studt, J. Rossmeisl, J. K. Nørskov, *Energy Environ. Sci.* **2010**, *3*, 1311.
- [74] F. Calle-Vallejo, M. Huang, J. B. Henry, M. T. M. Koper, A. S. Bandarenka, *Phys. Chem. Chem. Phys.* **2013**, *15*, 3196.
- [75] J. Rossmeisl, A. Logadottir, J. K. Nørskov, *Chem. Phys.* **2005**, *319*, 178.
- [76] J. K. Nørskov, J. Rossmeisl, A. Logadottir, L. Lindqvist, J. R. Kitchin, T. Bligaard, H. Jonsson, *J. Phys. Chem. B* **2004**, *108*, 17886.
- [77] Q. Hu, Y. Qin, X. Wang, Z. Wang, X. Huang, H. Zheng, K. Gao, H. Yang, P. Zhang, M. Shao, C. He, *Energy Environ. Sci.* **2021**, *14*, 4989.